NRIAG JOURNAL OF ASTRONOMY AND GEOPHYSICS
2019, VOL. 8, NO. 1, 185–197
https://doi.org/10.1080/20909977.2019.1667130

Integrated image processing and GIS-based techniques using knowledge-driven approaches to produce potential radioactivity map for the uraniferous granite of Egypt

Mahinaz M. Shawky[a], Reda A. El-Arafy[a], Mohamed A. El Zalaky[a] and Taha Elarif[b]

[a]Remote Sensing and GIS Department, Nuclear Materials Authority, Cairo, Egypt; [b]Faculty of Computers and Information Sciences, Ain Shams University, Cairo, Egypt

ABSTRACT

Interpretation of remote sensing data for allocating of lithologic units and for mapping of radioactive zones, supplies a valuable utility to produce Potential Radioactivity Map for the uraniferous granite. The study applied a digital image processing technique including interpretation and manipulation of Geophysical Airborne gamma-ray spectrometry data and The Advanced Spaceborne Thermal Emission and Reflection Radiometer (ASTER) sensor image data of Terra satellite over a case study well-known radioactive area of El-Missikat, El-Eridya and Kab Amiri areas in the Central Eastern Desert, Egypt. The possible forms of digital image manipulation are categorised into the following procedures: Minimum Noise Fraction (MNF) rotation, colour composite, band ratios, Principle Component Analysis (PCA), decorrelation stretching and Iterative Self-Organising Data Analysis Technique Algorithm (Isodata) unsupervised classification. Matched Filter (MF) classification was performed on the data to map a chosen well- known alteration mineral association with the uranium occurrences from USGS library. Each of these constructed images with the surveyed Airborne spectrometry data (equivalent uranium) has been given a suitable weight to be integrated using Geographic Information System (GIS) tools to delineate the most promising potential radioactive zones. Moreover, the other comparatively and quantitatively goal of the study was to evaluate the performance of various knowledge-driven mineral probability modelling.

ARTICLE HISTORY
Received 26 March 2019
Revised 5 June 2019
Accepted 6 September 2019

KEYWORDS
Image processing; ASTER; airborne gamma-ray spectrometry; uranium mineralisation; GIS; potential map

1. Introduction

Remote sensing discusses the technology of gaining information about the earth's surface and atmosphere by spaceborne (satellites) or sensors on-board air-borne (aircraft) platforms (Hellman and Ramsey 2004). The Advanced Space-borne Thermal Emission and Reflectance Radiometer (ASTER) system consists of three sub-systems: (1) Visible and near infrared (VNIR) operating in 3 bands with 15 m spatial resolution; (2) Shortwave infrared (SWIR) operating in 6 bands with 30 m spatial resolution; (3) Thermal infrared (TIR) operating in 5 bands with 90 m spatial resolution. ASTER channels make it the best spaceborne tool for geology since 6 spectral bands in the SWIR range, allowing the identification of carbonates and good discrimination between alteration mineral, including clays and iron oxides (Abrams 2000; Yamaguchi and Naito 2003; Ninomiya et al. 2005).

Using MNF as a pre-processing technique to increase the capability of extracting information from ASTER data (Green et al. 1988; Shawky et al. 2019). Although, it is difficult to nominate the 3 bands that will give the best outcomes for extracting lithological information from ASTER data, The Optimum Index Factor (OIF) is a statistical value used to choose the optimum combination of 3-bands with the highest sum of standard deviations and least amount of duplication of the data input to produce a colour composite (Patel and Kaushal 2011). Statistical band selection relies on the fact that not all image bands carry the same amount of information and that adjacent bands in the spectral domain are highly correlated. The OIF technique simplifies that selection by quantitative evaluation of the scene statistics and avoids the time consumption of the visual analysis process of large numbers of potential RGB combination (Beauchemin and Fung 2001). Matched Filter (MF) classification was performed on the data to map a well- known chosen alteration mineral associated with the uranium occurrences such as: Kaolinite, Illite, Haematite and Chlorite, by matching endmember spectra of the image and their spectra from USGS library.

Naturally occurring radioactive elements occur in rock and soil near the earth's surface. Three elements, K, U and Th, are relevant to this research because they or their daughter products emit gamma radiation that can be measured by air-borne gamma-ray spectrometer (AGRS) techniques (IAEA 1991).

CONTACT Reda A. El-Arafy reesmat@gmail.com Nuclear Materials Authority, P.O. Box 530, El-Maadi, Cairo, Egypt

Typically, the main component of gamma-ray flux is contained within the upper 30 cm of the Earth's surface (Wilford 2002). The airborne gamma-ray spectrometry has specific three windows (channels) in order to record the radiation emitted by the radionuclides K^{40}, U^{238} and Th^{232} (IAEA 2003). Geographic information systems (GIS) and image processing systems can be used as powerful tools to integrate gamma-ray images with other datasets such those derived from satellite SPOT, Landsat TM or ASTER sensors (El Arafy 2016). Although airborne gamma-ray surveys cover large swaths of ground, there are several limitations to this technique. Furthermore, not all radioisotopes are in equilibrium in surficial materials that emit gamma-rays collected during airborne surveys. Therefore, gamma-ray data for regolith mapping and radioelement exploration is best used together with other datasets including satellite remote sensing techniques (El Arafy 2016).

The current methods of mineral exploration utilising geophysical tools alone are expensive and time-consuming; therefore, it is needed to exploit recent tools of RS and GIS in the mineral exploration (Arnous 2016). These tools are extremely fast and effective in producing and modelling valuable data in various environmental research and Geoscience fields such as geology and geomorphology, and in detecting and mapping the probable sites of the minerals (Arnous 2016). Several radioactive anomalies with visible yellow secondary uranium mineralisation along founded at the northern fringe of G. El-Missikat and the southern fringe of G. El-Eridiya plutons of the study area (Figure 1). These anomalies are associated with highly brecciated greyish black and red jasper filling fractures and shear zones. The mineralised shear zones have specific alteration features as silicification, hematitization and kaolinisation (Abdelrahman 2014; Shawky et al. 2019). Discriminating alteration zones of kaolinite, Illite, Haematite and Chlorite as the main types of hydrothermally altered minerals using spectra derived from the imagery and from the library of the U. S. Geological Survey (USGS).

The areas that used as a case study area to apply the techniques are El-Missikat-El-Eridiya-Kab Amiri districts lies in the Central Eastern Desert of Egypt (Figure 1). It represents an important example of younger granites (monzogranite and syenogranite) within the Arabian Nubian Shield. Airborne gamma-ray spectrometry revealed that the syenogranitic bodies have the highest radioactivity related to shear zones usually filled with silica veins and an abnormal radioactivity with visible uranium mineralisation they are denser and closely spaced in the northern granitic mass of G. El-Missikat than those at the southern mass of G. El-Eridiya (Elsaid et al. 2014). Several geological studies have been investigated the area and showing its radioactivity importance (Ammar

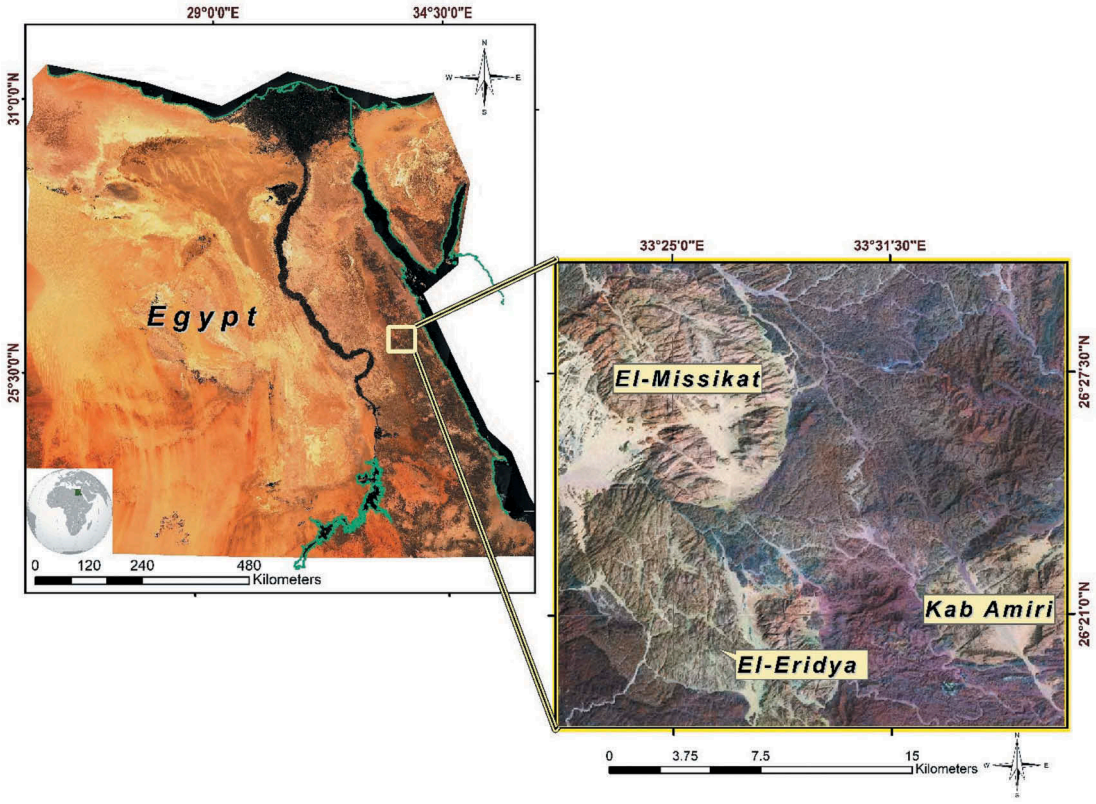

Figure 1. Location map of Egypt showing the selected areas of investigation.

1973; Bakhit 1978; El Tahir 1985; Abu Dief 1993; El-Mansi 1993; Moghazi 2002; Gaafar and Aboelkhair 2014)

The aim of this study is to combine and to analyse the previous generated spatial data layers (ASTER imagery, Airborne gamma-rays and minerals' reflectance spectrometry) using mathematical and quantitative data models and to produce potential radioactivity zones for the discriminated uraniferous granite of El-Missikat, El-Eridya and Kab Amiri areas in the Central Eastern desert, that will assist in the further mineral exploration and evaluation studies. ASTER L1B and Airborne gamma-ray spectrometry data were integrated in this study.

2. Data and methods

The dataset in this study consists of ASTER level-1B (L1B) and Airborne gamma-ray spectrometry data. The case study area is located between 33.36066389 to 33.67515000 longitudes and 26.52412222 to 26.31346389 latitudes. ASTER data acquired on 7/10/2007 and geocoded to the UTM projection (WGS 84 – Zone 38 N). Radiometrically and geometrically corrected radiance at sensor ASTER L1B (Granule: ASTL1B_071007_083611_080912_0036) covers the whole region has been used in this study.

ASTER L1B data are registered radiance-at-the-sensor product contains radiometrically calibrated and geometrically co-registered data. Cross-talk correction was applied to the ASTER data using Cross-talk Correction Software provided by Earth Remote Sensing Data Centre (ERSDAC); to remove the effects of energy leaking from band 4 into bands 5 and 9 (Gozzard 2006; Hashim et al. 2011; Van der Meer et al. 2012; Wahi et al. 2013; Jing et al. 2014; Khaleghi et al. 2014; Pournamdari and Hashim 2014; Pournamdari et al. 2014; Kumar et al. 2015). Three visible and near-infrared (VNIR) bands between 0.52 and 0.86 μm and six short-wave infrared (SWIR) bands from 1.6 to 2.43 μm, were stacked, resampled and registered to 15m resolution forming 9 bands using the nearest neighbour method.

An airborne gamma-ray geophysical survey of the study area was carried out by Aero-Service, Western Geophysical Company of America, in 1984 designated as an area – IB (Aero Service Report 1984). Airborne radiometric data measure the gamma-ray flux above the earth's surface, produced by the radioactive decay of Uranium, Thorium and Potassium. Airborne data projected to Egypt Red Belt Transverse Mercator, Helmert 1906. Such that Latitude of natural origin is 30°, Longitude of natural origin is 31°, False easting is 615000m and False northing is 810000m; then rasterized and spatially resampled to a 15m resolution to be compatible with ASTER data. The airborne radiometric data were processed to show the distribution of Uranium (eU), Thorium (eTh) and Potassium (^{40}K) in the study area. Airborne radiometric data are suitable for geological research and mineral exploration. Aerial gamma-ray surveys easily detect Granites; The method may not directly identify mineralisation but can act as an auxiliary method in locating potentially mineralised systems (Hyvönen et al. 2005).

ENVI 5.3 and IDL 8.5, MATLAB R2016b and ArcGIS 10.5 software were used to process the ASTER imagery and Airborne data, and preparation of GIS layers respectively. Figure 2 represents the steps of the proposed processes as a logistic conceptual model.

2.1. ASTER data

As a preprocessing procedure for ASTER L1B, radiance data were atmospherically corrected and converted to surface reflectance using Internal Average Relative Reflectance (IARR).

2.1.1. Minimum noise fraction (MNF)

MNF is a preprocessing and transformation technique for denoising image data. It transforms noisy data into components with decreasing noise fraction. The Minimum Noise Fraction (MNF) transform is an algorithm involving two successive data reduction operations. The first is based on an evaluation of noise in the data characterised by a correlation matrix. MNF transformation decorrelates the data and rescales the noise in the data, by variance. The second accounts for the original correlations, and produces a set of components that have weighted information concerning the variance through all bands in the original data set. The algorithm preserves specific channel information for each components' weighting of all original bands. The first few surface reflectance variations of MNF bands contain signal, while the remaining bands contain noise (Green et al. 1988; Vermillion and Sader 1999).

MNF transforms bands from the original space to eigenspace. The data space can be represented as two parts: one-part accompanying with large eigenvalues and coherent eigenimages, and the other part with near-unity eigenvalues and noise-dominated images. By using the coherent portions only, separating noise from the data, hence improving spectral processing results (Vermillion and Sader 1999; Hashim et al. 2011; Berman et al. 2012; Lasaponara and Masini 2012; Pour and Hashim 2012; Frassy et al. 2013). Bands with eigenvalues' value less than 2 were considered as a noise and then transform the MNF bands back to their original data space without noise band-(s) (Shawky et al. 2019).

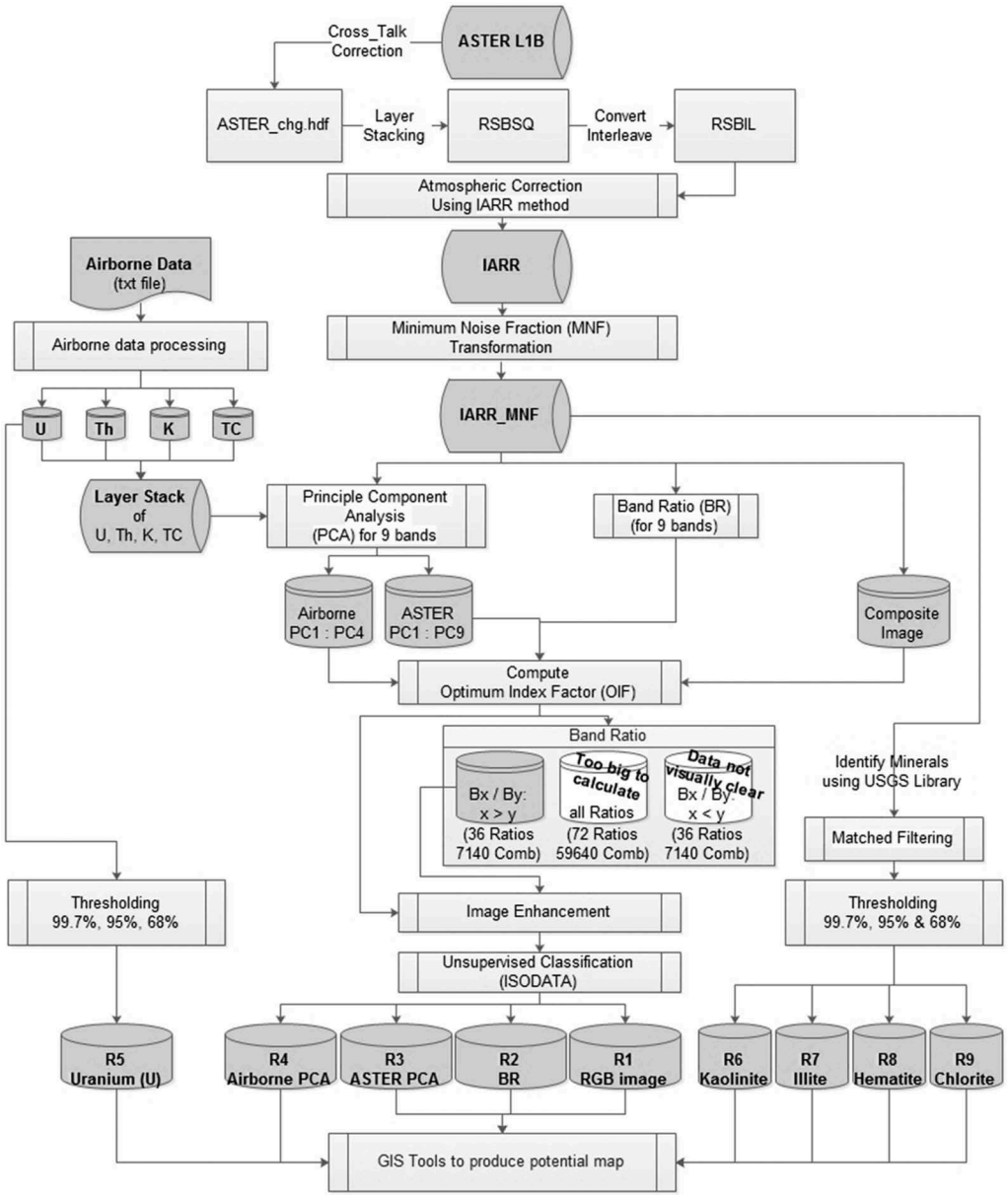

Figure 2. Steps of the proposed processes.

2.1.2. Band rationing (BR)

BR is a type of image enhancement. A Band ratio image is produced by dividing the corresponding digital number (DN) values of two bands and displaying the result as a greyscale image (Madani and Emam 2011; Pournamdari et al. 2014). Using band ratio images is better than using only individual bands to define and distinguish certain features that cannot be discriminated on a single band. All combinations of band ratios between the 9 bands are produced in a correlation matrix in three images. The first image contains all band ratios (36 bands) where the higher band number over the lower one (ex. B7/B5); the second image (36 bands) contains the lower over the higher band number (ex. B4/B9); and the last image contains all the band ratios (72 bands) contained in the previous two images.

2.1.3. Principle component analysis (PCA)

PCA is a linear transformation to reduce such information redundancy in multispectral images; which decorrelates multivariate input data by rotating and/or translating the axes of its original space, so that the data can be exemplified without correlation in a new space that should be capable to identify different features and surface types easier. In order to apply this: (i) the covariance matrix amongst all input spectrum bands was computed, then (ii) eigenvalues and eigenvectors were produced with the purpose of obtaining the new feature components. PCA is useful for enhancing the information content, segregating signal from noise, and reducing the dimensionality of datasets (Patel and Kaushal 2011; Lasaponara and Masini 2012; Liu and Mason 2013; Pournamdari et al. 2014; Kumar et al. 2015). Since the eigenvectors and

eigenvalues are computed from the covariance matrix, the PC transform maximises the data variance in the first few PC bands, these bands contain the greatest amount of the coherent image information and they can be used to isolate common features in the data. Often, higher-order PC images contain rare features and/or noise (Kumar et al. 2015).

2.1.4. Optimum index factor (OIF)

OIF is a common statistical method which was used to specify the best three band combinations and rank the bands according to their statistical information. It is based on the quantity of the total variance and correlation between various bands (Patel and Kaushal 2011; Pournamdari et al. 2014). Chavez et al. (1982) define a formula to calculate OIF by using three standard deviations and three correlation coefficients. The optimum combination of all possible 3-band combinations has the highest amount of information (= greatest sum of standard deviations), with the least amount of duplication (= lowest correlation among band pairs) (Ren and Abdelsalam 2001; Van der Meer et al. 2012; Bhattacharjee 2013).

For each combination of three bands, the OIF is calculated as (Patel and Kaushal 2011; Pournamdari et al. 2014; Jakob et al. 2015):

$$\mathrm{OIF} = \frac{\mathrm{Std_i} + \mathrm{Std_j} + \mathrm{Std_k}}{|\mathrm{Corr_{i.j}}| + |\mathrm{Corr_{j.k}}| + |\mathrm{Corr_{i.k}}|}$$

Where Std_i is the standard deviation of band i,

Std_j is the standard deviation of band j,

Std_k is the standard deviation of band k,

Corr_{ij} is the correlation coefficient between bands i and j,

Corr_{jk} is the correlation coefficient between bands j and k,

Corr_{ik} is the correlation coefficient between bands i and k.

Such that:

Standard Deviation (Std): $\sigma_x = \sqrt{\frac{1}{N}\sum_{i=1}^{N}(x_i - \bar{x})^2}$

where Nis the number of points and x-bar ($\bar{x}$) is the mean.

Correlation Coefficient: $Corr_{xy} = \frac{Cov\ (x.y)}{\sigma_x \sigma_y}$

Where σ_x and σ_y represent the standard deviation of x and y respectively;

Covariance: $cov(x, y) = \frac{\sum_{i=1}^{N}(x_i - \bar{x})(y_i - \bar{y})}{N - i}$

Such that: Cov(x,y) shows how two variables are related.

2.1.5. Decorrelation stretches

It is a method of image enhancement, which enhances the colour saturation of a colour composite image and thus effectively improves the visual quality of the image spectral information, without significant distortion of its spectral characteristics (Chang 2003; Liu and Mason 2013).

2.1.6. Image classification

It uses imagery to produce thematic maps. The goal of classification is to identify characteristic features, patterns or structures within an image and use these to assign them to a particular class (Chang 2003; Schott 2007; Solomon and Breckon 2011; Lasaponara and Masini 2012; Karakus and Karabork 2016). Unsupervised classification is accomplished without any previous knowledge of the image. ISODATA method group pixels into a pre-defined number of classes depending on their reflectance features. ISODATA calculates class means regularly circulated in the data before iteratively clusters the continuing pixels using least distance approaches. Every iteration recalculates means and reclassifies pixels according to the new recalculated means, Isodata automatically adjusts the number of clusters during the iteration by splitting clusters which have large standard deviation values and merging similar clusters (Abbas et al. 2016).

2.1.7. Matched filtering (MF)

MF technique was used as a signature target detection to find the profusions of user-defined endmembers and to help distinguish targets from background for mineral exploration. Multispectral imaging provides significant information about the spectral characteristics of materials in the surface of the Earth. Due to high spectral resolution, each pixel (deemed as a vector) can be seen as a "fingerprint" of the fundamental materials within the spatial point. Based on the spectral signatures, imaging has the extraordinary possibility to recognise small targets of interest. The targets are mainly man-made objects or objects with signatures being spectrally distinctive from image background, which are mostly embedded in a single pixel area and cannot be straightforwardly recognised by visual inspection. The major objective of target detection is to detect these targets by exploiting the spectral signatures of the materials (Gao et al. 2015). MF technique maximises the response of the known endmember and minimises the response of the unknown background, therefore matching the known signature; based on matches to spectral library or image endmember spectra and does not necessitate knowledge of all the endmembers within the image (Shawky et al. 2019). Choosing Kaolinite, Illite, Haematite and Chlorite to illustrate hydrothermal alteration zones; as the implanted pure target, whose standard spectrum was from the U.S. Geological Survey (USGS) Spectral Library and were then

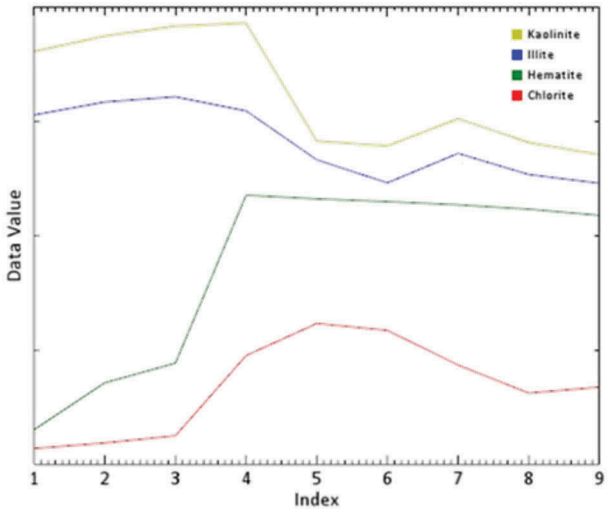

Figure 3. The spectra of the studied minerals from the USGS library.

resampled to match ASTER multispectral signatures. Figure 3 shows the spectra of the studied minerals from the USGS library. Matched Filtering technique was applied to the composite image after using MNF and removing the noise.

2.2. Airborne data

The preprocessing steps of airborne gamma-ray radiometric digital data are as follows:

(a) Rasterizing each element of eU, eTh, K and total count (TC) to convert the text data to an image file.
(b) Resampling and projecting the product images to Red Belt Projection with a pixel size 15x15m.
(c) Merging the four elements' images into one multi-bands image that can be manipulated and processed as an ordinary image.

These processes were essential to attain compatibility and coincidence between the different layers that can be extracted from ASTER and Airborne data and can be easily used in GIS modelling and techniques in a combination with the other layers.

2.3. Geographic information system (GIS)

GIS has gained increasing importance in the analysis and integration of spatial data layers. GIS provides a number of useful methodologies for viewing, organising, query, combining, analysing, estimating, evaluating and supporting decision-making(Kayadibi and Aydal 2017). Data-driven approaches require sufficient training data to represent well the spatial relationships between mineral formations and evidence maps. Knowledge-driven approaches can be used in areas where under-worked and known minerals are less or not sufficient as in the case of the present study area. These approaches are based on the expert opinion according to the conceptual model defined or the ore deposit model (Kayadibi and Aydal 2017). The predictive modelling methods include; weighted sum, weighted overlay and fuzzy logic.

Both Weighted sum and Weighted overlay weight combine multiple inputs to produce an integrated image; higher values indicate that a location is more suitable. The main difference is that Weighted Sum does not rescale the reclassified values to an evaluation scale and allows integer and floating-point values, while Weighted overlay allows only integer values (ESRI 2016; Kayadibi and Aydal 2017).

Fuzzy logic is an overlay analysis technique. It supposes that there are inaccuracies in the geometry and attributes of spatial data, that is inaccuracies of class boundaries. The Weighted Sum and Weighted Overlay tools are based on crisp sets, such that each cell belongs to a class or not. Fuzzy logic addresses states when the boundaries of classes are not clear; therefore, it defines possibilities, not probabilities (ESRI 2016). Fuzzy logic reclassifies the original values to the possibility that they belong to a defined set between 0 and 1 through MS Large function, where it depends on a specified mean and standard deviation. The midpoint is defined as a membership of 0.5 and the other values with greater or lower value compared with it which has higher or lower possibility of being a member of the set. The Fuzzy Overlay permits the study of the possibility of a member belonging to multiple sets in a multi-criteria overlay analysis (ESRI 2016; Kayadibi and Aydal 2017). Fuzzy Operators are:

- Fuzzy And: returns the minimum value of the sets.
  $$Fuzzy\ And\ Value = min\ (arg_1, \ldots, arg_n)$$
- Fuzzy Or: returns the maximum value of the sets.
  $$Fuzzy\ Or\ Value = max\ (arg_1, \ldots, arg_n)$$
- Fuzzy Product: multiplies each of the fuzzy values for all the input criteria for each cell. It is difficult to correlate the result to the relative relationship of the values.
  $$Fuzzy\ Product\ Value = product\ (arg_1, \ldots, arg_n)$$
- Fuzzy Sum: adds the fuzzy values of each set.
  $$Fuzzy\ Sum\ Value = 1 - product\ (1 - arg_1, \ldots, 1 - arg_n)$$
- Fuzzy Gamma:

It is a mathematical product of fuzzy Product and fuzzy Sum, such that both are raised to the exponential of gamma. If the specified gamma is 1,

the output is equal to the fuzzy Sum; if gamma is 0, the output is the same as a fuzzy Product.

*Fuzzy Gamma Value = pow ([1 – ((1 – arg_1) * (1 – arg_2) * …)], Gamma) * pow ([arg_1 * arg_2 * …], 1 – Gamma).*

3. Results and discussion

In this research study, ASTER L1B data were atmospherically corrected and converted to surface reflectance using IARR. Then, MNF transformation was applied to evaluate the noise in the data by transforming data images from normal space to eigenspace. MNF 1 represents the greatest variation while the smallest amount (1.5985) is noted at MNF 9. Most of the information (99.11%) of the total variability is obtained in the first 8 MNFs. Thus, MNF 9 will be essentially noises and need to be removed. Therefore, transform the MNF bands (MNF 1 to MNF 8) back to their original data space without MNF 9 to exclude the noise.

3.1. Conventional image processing techniques

The output ASTER data have 9 bands in VNIR and SWIR; the number of possible combinations of the three bands is determined as:

$$\binom{N}{3} = \frac{N!}{3!*(N-3)!}$$

Where N is the total number of bands; for the 9 bands, there are 84 combinations. OIF was calculated to compare between these combinations by ranking and sorting them from best to worst. The best 3-band combination of the colour composite image has been found bands 3, 7 and 8.

OIF was applied also to both Band Ratio Images created of ASTER data, and PCA of ASTER and Airborne gamma-ray images data. For the band ratios, all band combinations (36 bands) has been applied. In order to apply OIF, the number of possible 3 band combinations of 36 bands is 7140 combinations; OIF was calculated for these combinations. While for 72 bands there are 59,640 combinations which considered too big to be calculated and time consuming. The best 3-band combination of the band ratio image has been found 5/3, 8/1 and 9/4 to illustrate and identify the granitic rocks in the area. PCA for ASTER and Airborne gamma-ray images data has been produced. OIF was computed on the output results and the best 3-band combination of ASTER has been found PC 1, 2 and 9. These combinations are predictable to have the maximum amount of extractable lithological information for visual interpretation since they use bands with the least amount of redundancy in the remotely sensed data (Beauchemin and Fung 2001). After choosing the best 3-band combination of the processed data, decorrelation stretch was taken place as a process that is used to enhance the colour differences in the colour image; by removing the correlation of the input pixels.

To categorise all pixels of giving the image into classes; an image classification technique was used. Isodata unsupervised classification algorithm takes place to automatically groups the pixels into unknown or non-predefined classes. Choosing the appropriate parameters depended on experiment and how long consume in time of operation. The specified parameters used in this study was:

- Number of Classes from 5 to 10
- Minimum number of pixels in each class = 300 000
- Maximum class standard deviation = 1
- Minimum class distance = 100
- Maximum number of merge pairs = 5
- Maximum iterations = 10
- Threshold = 0.005

At this step, after a decorrelation stretch and Isodata, we have three outputs classified images that successfully showed the best discrimination for the granitic rocks' exposures and its alterations in the study area (Figure 4):

- ***R1***: for the 3-bands (3,7,8) composite of the original image after removing noise, – ***R2***: for the 3-bands (5/3, 8/1, 9/4) composite of band ratio image, – ***R3***: for the 3-bands (PC1, PC2, PC9) composite of PCA image.

3.2. Airborne spectrometry technique

The airborne gamma-ray spectrometric digital data (as text file contains 6 columns which represent X and Y coordinates, eU, eTh, K% and TC distribution) were converted to image format by rasterizing the point data. These images showed the intensity distribution of TC, eU, eTh (in ppm) and ^{40}K (percentage).

The resampling process was essential to guarantee the coincidence between the different layers that could be extracted from data (Airborne and ASTER). Combine the 4 distribution images into 1 image, compute PCA, then identify the best 3-bands combination using OIF. The best 3-bands combination of Airborne has been founded PC 1, 3 and 4 which represent U, K and TC. After that, apply decorrelation stretch and Isodata processes to the output image to classify the regions of fertile granites. Using the threshold (99%, 95% and 68%) to classify the distribution image for eU to produce a region of interest (ROI) which define the localisation of fertile granites in the area. The outputs of this step were (Figure 5):

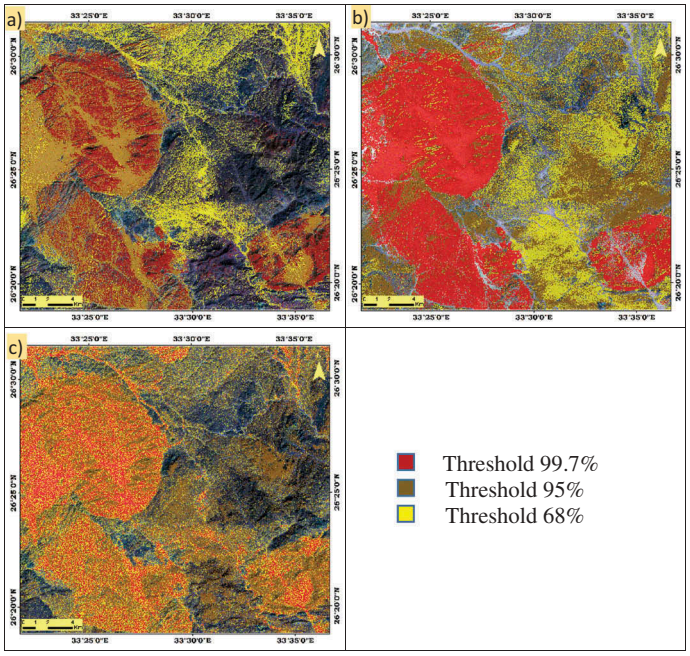

Figure 4. The output image layers: (a) Colour composite image **R1**, (b) Band ratio image **R2**, (c) PCA of ASTER image **R3.**

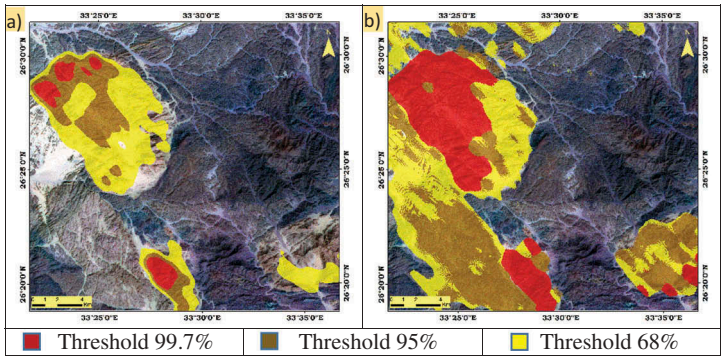

Figure 5. The output image layers: (a) Uranium distribution image from Airborne **R4**, (b) PCA of Airborne images **R5.**

- ***R4*** represents ROI of eU in the study area, – ***R5*** for the 3-bands (PC_U, PC_K, PC_TC) composite of PCA image.

3.3. Mineral spectral mapping

The last input parameters for the evaluation to produce the potentiality map for the fertile granite and radioactive zones in the study area was to map the minerals associated with the uraniferous granite. Each mineral has its own characteristic spectral absorption and reflection features. In this study, the used minerals are Kaolinite, Haematite, Illite and Chlorite. Using USGS library spectra to identify the high and low reflectance bands for each mineral in VNIR-SWIR bands of ASTER satellite data. The proposed minerals association was chosen according to the previous studies and observations in the area as the main association for the uranium mineralisation (El-Mansi 1993; Moghazi 2002; Abdelrahman 2014; Elsaid et al. 2014; Gaafar and Aboelkhair 2014). Matched Filtering (MF) algorithm was used to identify the alteration zones of the selected minerals using the USGS mineral reference spectra.

The results of this step were (Figure 6):

- ***R6*** distribution of Kaolinite, – ***R7*** distribution of Illite, – ***R8*** distribution of Haematite, – ***R9*** distribution of Chlorite.

As a result, at the final stage, nine different input (parameters) layers (R1 to R9) have been distinguished. All layers are compatible and coincidence to be transferred to GIS environment at the following stage.

3.4. Potential radioactivity map

All the previous output layers (parameters) from the different techniques and processes for both ASTER and

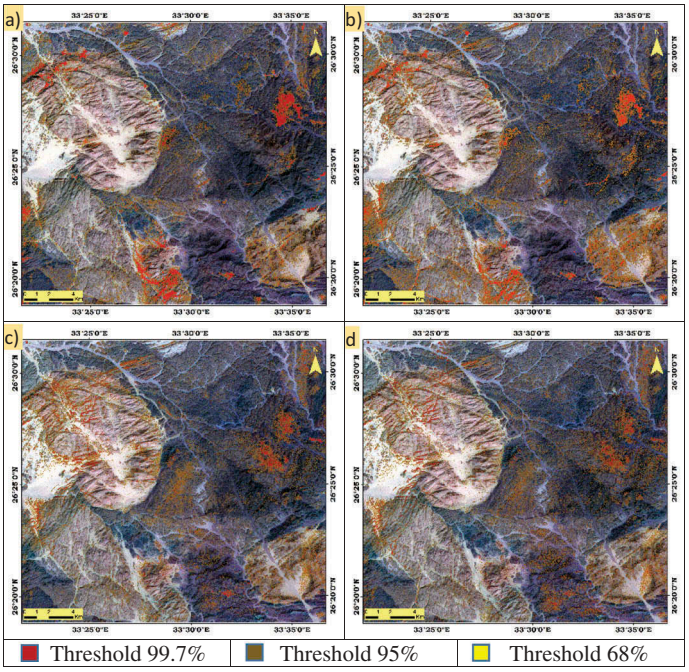

Figure 6. The output image layers: (a) Distribution of Kaolinite image **R6**, (b) Distribution of Illite image **R7**, (c) Distribution of Haematite image **R8**, (d) Distribution of Chlorite image **R9.**

Airborne data were reclassified and assigned ranks and weights (Figure 7 and Table 1). In this process, the thematic layers were ranked depending on the information embedded in each. The rank and weight of these layers were derived from the effects of each contribution approved to expert opinion based on the characteristics of the ore formation and identification criteria determined by the conceptual model. The order was set as the higher contribution to the target of radioactivity zones.

The weight of each layer has been calculated as the rank of it divided by the total number of ranks. Each layer classified into two to four classes: very high, high, moderate, and background. Similarly, the classes in each input layer were categorised and ranked from 0 to 3; where 3 is the best and 0 is the background; based on the ability to reserve data. The capacity value of data of each subclass was computed from the multiplication of the rank of it and the weight of its layer, then divide the result over the total ranks of classes.

A predictive mineral modelling process is performed by combining and analysing predictive layers using a function that characterises the interaction and relationships between the layers and the processes controlling the mineralisation system using three methods from knowledge-driven modelling approaches (Kayadibi and Aydal 2017). These methods include: weighted sum, weighted overlay and fuzzy logic. All of these output raster layers were used as a data layer in a GIS modelling and were used to predict the potential radioactivity map. Figure 7 represents the potential map correlation flowchart. Figure 8 shows the output potential maps from the different methods.

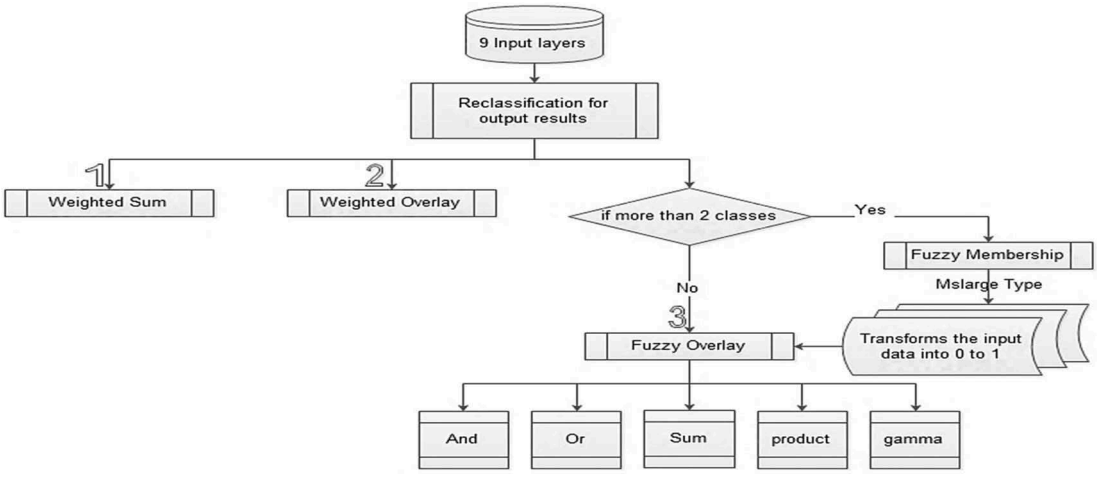

Figure 7. The potential map correlation flowchart.

Table 1. The thematic layers' weights and their capacity values.

Order	Name	Rank	Weight		Classes	Class Rank	Capacity value
1	PCA of Airborne	22	0.22	1	Background	0	0
				2	Moderate	1	0.03667
				3	High	2	0.07333
				4	Very high	3	0.11
					Sum	**6**	**0.22**
2	Airborne eq. Uranium	20	0.2	1	Background	0	0
				2	Moderate	1	0.03333
				3	High	2	0.06667
				4	Very high	3	0.1
					Sum	**6**	**0.2**
3	PCA of ASTER	15	0.15	1	Background	0	0
				2	High	1	0.15
					Sum	**1**	**0.15**
4	Band Ratio	10	0.1	1	Background	0	0
				2	High	1	0.1
					Sum	**1**	**0.1**
5	Kaolinite	7	0.07	1	Background	0	0
				2	Moderate	1	0.02333
				3	High	2	0.04667
					Sum	**3**	**0.07**
5	Illite	7	0.07	1	Background	0	0
				2	Moderate	1	0.02333
				3	High	2	0.04667
					Sum	**3**	**0.07**
5	Haematite	7	0.07	1	Background	0	0
				2	Moderate	1	0.02333
				3	High	2	0.04667
					Sum	**3**	**0.07**
5	Chlorite	7	0.07	1	Background	0	0
				2	Moderate	1	0.02333
				3	High	2	0.04667
					Sum	**3**	**0.07**
6	Band composite	5	0.05	1	Background	0	0
				2	Moderate	1	0.01667
				3	High	2	0.03333
					Sum	**3**	**0.05**
	Sum	**100**	**1**				**1**

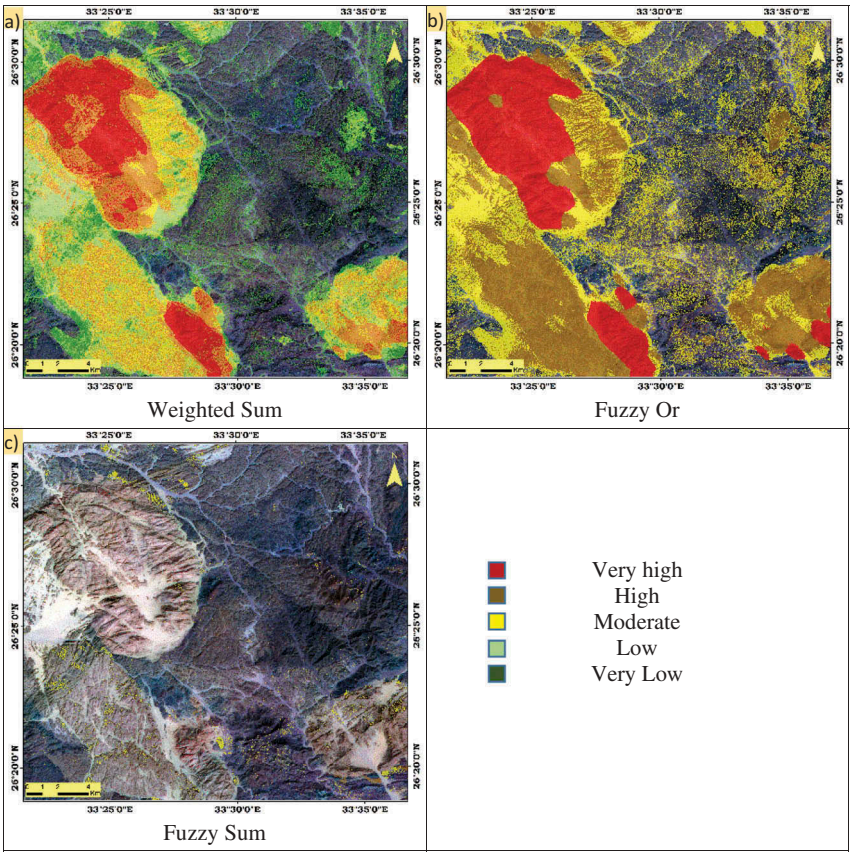

Figure 8. The final potential maps output from the different methods.

The Weighted sum method produces potential radioactivity map for the uraniferous granite of Egypt confirmed by the previous studies. Where it shows uraniferous granite location at North of El-Missikat, North of El-Eridya and South of Kab Amiri areas in the Central Eastern desert.

Gamma (γ) value was selected as 0.7 and 0.9 for the combination of the input layers using the Fuzzy Gamma operator. Nevertheless, the results were found very poor.

Fuzzy Or method gives good results in discrimination of fertile granites in the area when it runs without fuzzy membership transformation. On the other hand, Fuzzy Sum without fuzzy membership transformation recognises the mineralisation areas. While the other methods did not give representative results. The output images will lead the delineation of target areas, the identification of new targets for mineral exploration, evaluation work and radioactive deposit exploration.

4. Conclusion

The study applied an integration of the processed airborne gamma-ray spectrometry and satellite remote sensing data in a GIS environment to produce radioactive maps for The Uraniferous Granite in the study area. ASTER L1B data were atmospherically corrected and converted to surface reflectance using IARR method which is a useful method for the purposes of geological exploration. MNF transformation was used to eliminate the noise in the data with eigenvalue less than 2. A set of conventional image processing techniques and methods has been performed on data such as band ratios, PCA, OIF and unsupervised classification. Band ratio was created and used as an image enhancement to distinguish certain features that cannot be discriminated on a single band. PCA performed on data to reduce information redundancy in the images. Therefore, the data can be represented without correlation in a new space to identify and distinguish different surface features clearly. OIF applied as a statistical method to specify the best three band combinations and rank the combinations according to highest standard deviations and lowest correlation coefficients between bands. ISODATA Unsupervised classification was used to produce thematic maps. ISODATA algorithm is iterative procedures to automatically groups the pixels into unknown or non-predefined classes based on specified parameters like the minimum class distance value, the standard deviation within each class and the distance between classes centres.

The study demonstrates the results and importance of airborne radiometric as well as the suitability of remote sensing technique and GIS for exploration for radioactive materials. GIS model was used to rank and weight the output thematic layers depending on the information embedded in each. A predictive mineral modelling process is performed by combining and analysing the ranked layers to characterise the interaction and relationships between the layers using weighted sum, weighted overlay and fuzzy logic (fuzzy logic includes Fuzzy-and, Fuzzy-or, Fuzzy-product, Fuzzy-sum and Fuzzy-gamma) methods to output potential maps for the most promising areas that identify uraniferous granite. Weighted sum, Fuzzy-or and Fuzzy-sum grant the best outcomes. The results showed higher potentiality in areas of north El-Missikat, North of El-Eridya and South of Kab Amiri. On the other hand, the results showed moderate to low potentiality in areas of southeast El-Missikat, west El-Eridya and north of Kab Amiri areas. In addition to locations of the mineralisation areas.

The study proposed a detailed flowchart technique and processes for producing a potential radioactivity map in the study area and areas with similar conditions (arid – semi-arid regions). The output images and layers will guide the delineation of target areas in a broad search area, the identification of new targets for future detailed mineral exploration and evaluation work, and the study for new mineral deposit exploration.

Disclosure statement

No potential conflict of interest was reported by the authors.

ORCID

Mahinaz M. Shawky http://orcid.org/0000-0002-2280-3870

References

Abbas AW, Minallh N, Ahmad N, Abid SAR, Khan MAA. 2016. K-Means and ISODATA clustering algorithms for landcover classification using remote sensing. Sindh Univ Res J-SURJ (Sci Series). 48:2.

Abdelrahman MEH. 2014. The application of thermal remote sensing imagery for studying uranium mineralization: A new exploratory approach for developing the radioactive potentiality at El-Missikat and El-Eridiya district, Central Eastern Desert. Egypt: Damietta University.

Abrams M. 2000. The advanced spaceborne thermal emission and reflection radiometer (ASTER): data products for the high spatial resolution imager on NASA's Terra platform. Int J Remote Sens. 21(5):847–859.

Abu Dief A 1993. The relation between the uranium mineralization and tectonics in some Pan-African granite, west of Safaga, Eastern Desert, Egypt {PhD Thesis]. Assuit University.

Aero Service Report. 1984. Training course in airborne magnetic and radio-metric surveying. Presented to the Egyptian General Petroleum Corporation; Cairo (Egypt).

Ammar A 1973. Application of aerial radiometry of the geology of Wadi El-Gidami area, Eastern Desert [Unpublished Ph D Thesis 424~, Faculty of Science]. Cairo.

Arnous MO. 2016. Groundwater potentiality mapping of hard-rock terrain in arid regions using geospatial modelling: example from Wadi Feiran basin, South Sinai, Egypt. Hydrogeol J. 24(6):1375–1392.

Bakhit F 1978. Geology and radioactive mineralization of G. El Missikat area, Eastern Desert, Egypt [Ph. D. Thesis]. Cairo: Ein Shams Univ.

Beauchemin M, Fung KB. 2001. On statistical band selection for image visualization. PE & RS- Photogramm Eng Remote Sens. 67(5):571–574.

Berman M, Phatak A, Traylen A. 2012. Some invariance properties of the minimum noise fraction transform. Chemometr Intell Lab Syst. 117:189–199.

Bhattacharjee D. 2013. Optimum index factor (OIF) for landsat data: a case study on Barasat Town, West Bengal, India. Int J Remote Sens & Geosci (IJRSG). 2 (5):11–17.

Chang C-I. 2003. Hyperspectral imaging: techniques for spectral detection and classification. Vol. 1. Springer Science & Business Media. New York: Kluwer Academic/Plenum Publishers.

Chavez P, Berlin GL, Sowers LB. 1982. Statistical method for selecting landsat MSS. J Appl Photogr Eng. 8 (1):23–30.

El Arafy RA. 2016. Discrimination of various rock units in Abu Zenima area, Southwestern Sinai, Egypt, with emphases to the radioactive areas using the hyperspectral remote sensing and GIS techniques. Birmingham, Alabama: The University of Alabama at Birmingham.

El Tahir M 1985. Radioactivity and mineralization of granitic rocks of El Erediya occurrence and comparison to El Missikat Rei El-Garra occurrence, Eastern Desert, Egypt [Unpublished Ph D thesis]. Al-Azhar University.

El-Mansi M. 1993. Petrology, radioactivity and mineralizations of Abu Gerida El-Erediya area. Eastern Desert (Egypt): Cairo Univ.

Elsaid M, Aboelkhair H, Dardier A, Hermas E, Minoru U. 2014. Processing of multispectral ASTER data for mapping alteration minerals zones: as an aid for uranium exploration in Elmissikat-Eleridiya granites, Central Eastern Desert, Egypt. Open GEOL J. 8:1.

ESRI AD. 2016. Release 10.2. 2. Redlands (CA): Environmental Systems Research Institute.

Frassy F, Dalla Via G, Maianti P, Marchesi A, Nodari FR, Gianinetto M. 2013. Minimum noise fraction transform for improving the classification of airborne hyperspectral data: two case studies. Hyperspectral image and signal processing: evolution in remote sensing (WHISPERS), 2013 5th Workshop on, Gainesville, Florida, 1–4.

Gaafar I, Aboelkhair H. 2014. Analysis of geological and geophysical datasets for radioelement exploration in Kab Amiri area, Central Eastern Desert, Egypt. Open GEOL J. 8:1.

Gao L, Yang B, Du Q, Zhang B. 2015. Adjusted spectral matched filter for target detection in hyperspectral imagery. Remote Sens. 7(6):6611–6634.

Gozzard JR. 2006. Image processing of ASTER multispectral data. Perth, Australia: Geological Survey of WA.

Green AA, Berman M, Switzer P, Craig MD. 1988. A transformation for ordering multispectral data in terms of image quality with implications for noise removal. IEEE Trans Geosci Remote Sens. 26(1):65–74.

Hashim M, Pournamdary M, Pour AB. 2011. Processing and interpretation of advanced space-borne thermal emission and reflection radiometer (ASTER) data for lithological mapping in ophiolite complex. Int J Phys Sci. 6(28):6410–6421.

Hellman MJ, Ramsey MS. 2004. Analysis of hot springs and associated deposits in Yellowstone National Park using ASTER and AVIRIS remote sensing. J Volcanol Geotherm Res. 135(1–2):195–219.

Hyvönen E, Turunen P, Vanhanen E, Arkimaa H, Sutinen R. 2005. Airborne gamma-ray surveys in Finland. Geol Surv Finland Spec. Paper(39):119–134.

[IAEA] International Atomic Energy Agency. 1991. Airborne gamma ray spectrometer surveying. Vienna, Austria: International Atomic Energy Agency.

[IAEA] International Atomic Energy Agency. 2003. Guidelines for radioelement mapping using gamma ray spectrometry data.

Jakob S, Bühler B, Gloaguen R, Breitkreuz C, Eliwa HA, El Gameel K. 2015. Remote sensing based improvement of the geological map of the Neoproterozoic Ras Gharib segment in the Eastern Desert (NE–egypt) using texture features. Journal of African Earth Sciences. 111:138–147.

Jing C, Bokun Y, Runsheng W, Feng T, Yingjun Z, Dechang L, Suming Y, Wei S. 2014. Regional-scale mineral mapping using ASTER VNIR/SWIR data and validation of reflectance and mineral map products using airborne hyperspectral CASI/SASI data. Int J Appl Earth Obs Geoinf. 33:127–141.

Karakus P, Karabork H 2016. Effect of pansharpened image on some of pixel based and object based classification accuracy. International archives of the photogrammetry, remote sensing and spatial information sciences, Prague, Czech Republic, p. 7.

Kayadibi Ö, Aydal D. 2017. A comparative predictive analysis of weighted overlay, weighted sum and fuzzy logic for mineral prospectivity mapping of precious and base metal mineralizations at north-east of Gümüşhane city. NE Turkey: Geocarto International; p. 1–21.

Khaleghi M, Ranjbar H, Shahabpour J, Honarmand M. 2014. Spectral angle mapping, spectral information divergence, and principal component analysis of the ASTER SWIR data for exploration of porphyry copper mineralization in the Sarduiyeh area, Kerman province, Iran. Applied Geomatics. 6(1):49–58.

Kumar C, Shetty A, Raval S, Sharma R, Ray PC. 2015. Lithological discrimination and mapping using ASTER SWIR Data in the Udaipur area of Rajasthan, India. Procedia Earth Planet Sci. 11:180–188.

Lasaponara R, Masini N. 2012. Satellite remote sensing: a new tool for archaeology. Vol. 16. New York: Springer Science & Business Media.

Liu JG, Mason PJ. 2013. Essential image processing and GIS for remote sensing. London, UK: John Wiley & Sons.

Madani A, Emam A. 2011. SWIR ASTER band ratios for lithological mapping and mineral exploration: a case study from El Hudi area, southeastern desert, Egypt. Arabian J Geosci. 4(1–2):45–52.

Moghazi A. 2002. Petrology and geochemistry of Pan-African granitoids, Kab Amiri area, Egypt–implications for tectonomagmatic stages in the Nubian Shield evolution. Mineral Petrol. 75(1–2):41–67.

Ninomiya Y, Fu B, Cudahy TJ. 2005. Detecting lithology with Advanced Spaceborne Thermal Emission and Reflection Radiometer (ASTER) multispectral

thermal infrared "radiance-at-sensor" data. Remote Sens Environ. 99(1–2):127–139.
Patel N, Kaushal B. 2011. Classification of features selected through optimum index factor (OIF) for improving classification accuracy. J For Res. 22(1):99–105.
Pour AB, Hashim M. 2012. Identifying areas of high economic-potential copper mineralization using ASTER data in the Urumieh–dokhtar Volcanic Belt, Iran. Adv Space Res. 49(4):753–769.
Pournamdari M, Hashim M. 2014. Detection of chromite bearing mineralized zones in Abdasht ophiolite complex using ASTER and ETM+ remote sensing data. Arabian J Geosci. 7(5):1973–1983.
Pournamdari M, Hashim M, Pour AB. 2014. Spectral transformation of ASTER and Landsat TM bands for lithological mapping of Soghan ophiolite complex, south Iran. Adv Space Res. 54(4):694–709.
Ren D, Abdelsalam M 2001. Optimum index factor (OIF) for ASTER data: examples from the Neoproterozoic Allaqi Suture, Egypt. Proceeding of the geological society of America (GSA), annual meeting, Boston, USA, Paper. (123-0).
Schott JR. 2007. Remote sensing: the image chain approach. 2nd ed. Oxford, New York: Oxford University, Press Inc
Shawky MM, El-Arafy RA, El Zalaky MA, Elarif T. 2019. Validating (MNF) transform to determine the least inherent dimensionality of ASTER image data of some uranium localities at Central Eastern Desert, Egypt. J Afr Earth Sci. 149:441–450.
Solomon C, Breckon T. 2011. Fundamentals of digital image processing: a practical approach with examples in Matlab. London, UK: John Wiley & Sons.
Van der Meer FD, Van der Werff HM, Van Ruitenbeek FJ, Hecker CA, Bakker WH, Noomen MF, Van Der Meijde M, Carranza EJM, De Smeth JB, Woldai T. 2012. Multi-and hyperspectral geologic remote sensing: A review. Int J Appl Earth Obs Geoinf. 14(1):112–128.
Vermillion SC, Sader SA 1999. Use of the minimum noise fraction (MNF) transform to analyze airborne visible/infrared imaging spectrometer (AVIRIS) data of northern forest types. AVIRIS workshop.7, Pasadena, California.
Wahi M, Taj-eddine K, LaftouhI N. 2013. ASTER VNIR & SWIR band enhancement for lithological mapping-a case study of the Azegour Area (Western High Atlas, Morocco). ASTER. 3(12):33–45.
Wilford J. 2002. Airborne gamma-ray spectrometry. Cooperative research centre for landscape environments and mineral exploration, commonwealth scientific and industrial research organization, Bertley, WA. Aust Open File Rep. 144:46–52.
Yamaguchi Y, Naito C. 2003. Spectral indices for lithologic discrimination and mapping by using the ASTER SWIR bands. Int J Remote Sens. 24(22):4311–4323.